Dalton Transactions

ROYAL SOCIETY OF CHEMISTRY

PAPER

View Article Online
View Journal | View Issue

Check for updates

Cite this: *Dalton Trans.*, 2024, **53**, 9526

Structural and vibrational properties of lanthanide Lindqvist polyoxometalate complexes†

Primadi J. Subintoro and Korey P. Carter *

Received 15th March 2024,
Accepted 4th May 2024

DOI: 10.1039/d4dt00786g

rsc.li/dalton

Molecular spin qubits have demonstrated immense potential in quantum information science research due to the addressability of electron spins using microwave frequencies, and the scalability and tunability of molecular systems. Exemplary in this regard is the holmium polyoxometalate, $[Na_9Ho(W_5O_{18})_2]\cdot 35H_2O$ (HoW_{10}), which features an accessible atomic clock transition at 9.4 GHz; however, the coherence time of this molecule is limited by spin-phonon coupling driven decoherence processes. To limit these decoherence pathways, materials need to be designed to reduce energy overlap between spin and phonon states, and this necessitates developing a better understanding on how structural modifications impact the vibrational landscape for classes of complexes. Herein we conducted a full investigation into the fundamental structural and vibrational properties of the lanthanide Lindqvist polyoxometalate series, $[Na_9Ln(W_5O_{18})_2]\cdot xH_2O$ (Ln = La(III)–Lu(III), except Pm(III)) (LnW_{10}), to assess how structural changes effect vibrational characteristics and to elucidate pathways to improve the coherence properties of HoW_{10}. Single crystal X-ray diffraction results revealed four distinct structural polymorphs in complexes **1–14** wherein first coordination spheres were identical, and differences manifested as changes in lattice packing. Interestingly, the subtle changes in packing exhibited by the four polymorphs were found to impact distortions away from ideal D_{4d} symmetry for each of the LnW_{10} complexes. Raman and far-infrared (FIR) spectra of complexes **1–14** were collected to identify vibrational modes present in low energy regions and peak fitting assignments were made according to literature precedents. Qualitative and Partial least squares (PLS) analysis show correlations between complex structural parameters with the low energy Raman and FIR vibrational modes of interest. Overall, this investigation shows that the second coordination sphere plays an integral role in modulation of the structural and vibrational characteristics of LnW_{10} complexes, which makes it a viable route for tuning spin and vibrational manifolds of species within this series.

Introduction

Polyoxometalates (POMs) are the molecular counterparts of metal oxide materials that are comprised of oxygen and transition metals in their highest oxidation state usually from groups five and six (V, Nb, Ta, Mo, and W).[1,2] POMs form clusters with nuclearities ranging from 2–368 metal centers in contrast to the one, two, and three dimensional coordination networks formed in metal oxide materials. The topological diversity of POMs stems from the tunability of their self-assembly processes, wherein the controlled acidification or basification of MO_4^- (M = W, Mo, Nb, V, Ta) anions in aqueous media results in a nearly limitless array of structures.[3,4] The d^0 electronic configuration of the highest oxidation state group five and six transition metals as well as the high nuclearity and ability of POMs to coordinate with p-, d-, and f-block metals facilitates unparalleled electronic tunability that gives rise to interesting magnetic, optical, and redox properties.[1,3–12] This is exemplified by f-element POMs, wherein coordination of lanthanides and actinides with POM ligands has yielded materials with applications ranging from molecular spintronics and quantum information science (QIS) to medical imaging and catalysis.[13–19] In QIS, f-element POMs have been investigated as materials that can act as quantum bits (qubits), which are two-level quantum systems with the ability to

Department of Chemistry, University of Iowa, Iowa City, IA 52242, USA.
E-mail: korey-carter@uiowa.edu

†Electronic supplementary information (ESI) available: Crystallographic parameters for complexes **1–14**, additional structural figures, methodological details for determining structural distortion parameters, raw and fitted FIR and Raman spectra for complexes **1–14**, plots comparing structural distortion parameters *versus* lanthanide ionic radii, plots comparing FIR and Raman vibrational modes frequencies with structural distortion parameters, methodological details for performing PLS analysis, and plots produced from PLS analysis where the relationship between FIR and Raman vibrational modes frequencies and structural distortion parameters was investigated. CCDC 2336257 (complex **9** (DyW_{10})), 2336260–2336262 (complexes **3** (PrW_{10}), **8** (TbW_{10}), and **12** (TmW_{10})), 2336274–2336276 (complexes **5** (SmW_{10}), **6** (EuW_{10}), and **13** (YbW_{10})), 2336278 (complex **7** (GdW_{10})), 2336280 (complex **11** (ErW_{10})), 2336284 (complex **1** (LaW_{10})), 2336286 (complex **2** (CeW_{10})), 2336288 (complex **14** (LuW_{10})), 2336290 (complex **4** (NdW_{10})), and 2336921 (complex **10** (HoW_{10})). For ESI and crystallographic data in CIF or other electronic format see DOI: **https://doi.org/10.1039/d4dt00786g**

initiate and maintain a coherent superposition state of both quantum levels.[15,16,20–22] Electron spin based systems, such as f-element POMs, have tremendous potential to act as qubits and this has been demonstrated in two complexes, $[Ho(W_5O_{18})_2]^{9-}$ (HoW_{10}) and $[GdP_5W_{30}O_{110}]^{12-}$ (GdW_{30}), which feature an extended coherence time in a magnetically noisy environment, HoW_{10}, and the ability to facilitate implementation of multiple qubit transitions within a single compound, GdW_{30}.[23,24]

The extended coherence time in HoW_{10} is made possible by atomic clock transitions within the molecule,[24] which are avoided level crossings with zero Zeeman slope that result from wavefunction mixing of metal-ion spin states.[25] Clock transitions are a topic of significant research interest within the field of QIS due to decoupling of the coherent spin states from the surrounding magnetic environment at clock transition frequencies, which protects from spin–spin coupling based decoherence that can result from local magnetic induction.[26] The clock transitions in HoW_{10} stem from hyperfine and crystal field induced mixing that removes the degeneracy of the M_J = ±8 ground state multiplet for Ho(III), yielding instead a tunnel split pseudodoublet of M_J = ±4 ground states.[27–29] At the clock transition in HoW_{10}, coherence times were enhanced by four times to over 8 μs, and the clock transition also allowed for coherence to be achieved without significant matrix dilution of the paramagnetic metal centers, which is crucial for the potential scalability of the system for QIS applications. A drawback of the HoW_{10} system is that the spin–lattice relaxation time limited the coherence time for the complex, even at low temperatures (<10 K).[24,28,30] Spin–lattice relaxation times are governed by thermally activated processes involving spin states, and the changes as a function of temperature of coherence times for HoW_{10} indicated that the accelerated relaxation for this complex was a result of phonon coupling with the spin bath.[31,32] Prolonging spin–lattice relaxation times by minimizing spin–phonon coupling is a significant synthetic challenge as it involves manipulation of the vibrational landscape to limit energy overlap between metal-ion spin states and vibrational phonons.[31] In f-element POM systems, such as HoW_{10}, this necessitates the development of a fundamental understanding of the active vibrational modes for metal–POM complexes and requires delineation of structure–property relationships so that a handle can be developed on how changes in f-element coordination environments affect active vibrational modes and the crystal field splitting of spin states. Despite multiple studies focusing on lanthanide Lindqvist POM complexes, $[Ln(W_5O_{18})_2]^{9-}$ (LnW_{10}), there is limited understanding on how structural and vibrational spectroscopy characteristics of these complexes are related, even for HoW_{10}, and there has not been a systematic structural study covering the entire LnW_{10} series.[27,33–38]

Herein we describe our findings from comprehensive structural and vibrational spectroscopy studies we conducted on the complete lanthanide Lindqvist POM series, $[Na_9Ln(W_5O_{18})_2]\cdot xH_2O$ (LnW_{10}) (Ln = La(III)–Lu(III), except for Pm(III)). Single crystal X-ray diffraction results indicate that the entire series (complexes **1–14**) is isostructural, and all structures crystallize in the triclinic $P\bar{1}$ space group. There are structural differences within the LnW_{10} series though, as four different polymorphs were observed, three of which had not been previously identified. Differences between LnW_{10} polymorphs led to variations in the distortions from ideal D_{4d} symmetry for each complex, which suggested that first and second coordination sphere structural characteristics play a significant role in modulating metal-ion point group symmetry.[27,39,40] Distortions from ideal symmetry can modulate spectroscopic properties of LnW_{10} complexes and thus, understanding how structures have been distorted by changes in coordination chemistry and packing is pivotal to tune the vibrational landscape of these materials as the work of Shiozaki *et al.*[41] and Blockmon and colleagues[31] have illustrated. To achieve this aim, we collected both Raman and infrared (IR) spectra for the entire LnW_{10} series and subjected spectra to a peak fitting regime with the aim of definitively identifying the vibrational modes that were present, particularly in the low energy region (400–100 cm^{-1}) where peaks associated with spin–phonon coupling are generally observed.[24,42,43] Qualitative analysis of results showed polymorph specific trends when FIR [$\nu(WO_5)_2$, $\nu(LnO_8)$, and $\nu/\rho(LnO_8)$] and Raman [ν(Ln–O–W)] modes were compared to structural parameters such as ionic radii, skew angles, plane angles, and plane distances. Partial least squares (PLS) analysis confirmed the results from qualitative comparisons with the different structural parameters investigated here accounting for 37 to 86% of the variances observed in FIR and Raman vibrational modes. These results suggest tuning of structural characteristics may be a viable way to modulate the vibrational landscape of f-element POM complexes.

Experimental

Materials

All chemicals were purchased from commercial vendors and used as received. Lanthanum(III) nitrate hexahydrate ($La(NO_3)_3\cdot6H_2O$, 99.9%), cerium(III) chloride heptahydrate ($CeCl_3\cdot7H_2O$, 99%), neodymium(III) nitrate hexahydrate ($Nd(NO_3)_3\cdot6H_2O$, 99.9%), samarium(III) nitrate hexahydrate ($Sm(NO_3)_3\cdot6H_2O$, 99.9%), dysprosium(III) nitrate pentahydrate ($Dy(NO_3)_3\cdot5H_2O$, 99.9%), and holmium(III) nitrate pentahydrate ($Ho(NO_3)_3\cdot5H_2O$, 99.9%) were acquired from Beantown Chemical. Praseodymium(III) nitrate hexahydrate ($Pr(NO_3)_3\cdot6H_2O$, 99.9%), europium(III) nitrate hexahydrate ($Eu(NO_3)_3\cdot6H_2O$, 99.9%), gadolinium(III) nitrate hexahydrate ($Gd(NO_3)_3\cdot6H_2O$, ≥99.9%), terbium(III) nitrate hexahydrate ($Tb(NO_3)_3\cdot6H_2O$, 99+%), erbium(III) nitrate hydrate ($Er(NO_3)_3\cdot xH_2O$, 99.9%), ytterbium(III) nitrate pentahydrate ($Yb(NO_3)_3\cdot5H_2O$, 99.9%), and sodium tungstate dihydrate ($Na_2WO_4\cdot2H_2O$, 99+%, ACS grade) were acquired from Strem Chemicals, Inc. Thulium(III) nitrate hexahydrate ($Tm(NO_3)_3\cdot6H_2O$, 99.9%) and lutetium(III) nitrate hydrate($Lu(NO_3)_3\cdot xH_2O$, ≥99.9%) were acquired from Thermo Scientific. 70% nitric acid (ACS grade) was acquired from Sigma-Aldrich

and then diluted to a concentration of 0.5 M using Milli-Q H_2O.

Methods

Synthesis of $[Na_9Ln(W_5O_{18})_2]\cdot xH_2O$ (complexes 1–14). Each lanthanide Lindqvist POM was synthesized using the procedure published by Mariichak and colleagues.[33] Since the synthetic procedures for the entire $[Na_9Ln(W_5O_{18})_2]\cdot xH_2O$ series are identical except for the Ln(III) salt used, only a representative example, $[Na_9Ho(W_5O_{18})_2]\cdot 35H_2O$, will be discussed in detail. 0.625 mmol of $Na_2WO_4\cdot 2H_2O$ was dissolved in 5 mL of Milli-Q H_2O with magnetic stirring in a 10 mL round bottom flask and the tungstate solution was acidified with 1 mL of 0.5 M HNO_3 (2 mmol) solution, which was added at a rate of 100 μL per 30 s. Subsequently, 0.625 mL of 0.1 M $Ho(NO_3)_3\cdot 5H_2O$ (0.0625 mmol) solution was added to the acidified tungstate solution at a rate of 50 μL per 30 s until the solution became clear. The solution was then filtered with medium porosity filter paper into a plastic Petri dish and left to slowly evaporate in a 5 °C fridge for approximately one week. Rectangular plate and needle like crystals (color and shape of the crystal depend on the Ln(III) cation) were collected by filtration and washed with cold water. To improve crystal quality for X-ray diffraction studies, each sample was recrystallized *via* slow evaporation from hot water (90 °C) and crystals were kept in the mother liquor to prevent desolvation.

Characterization

X-ray structure determination. Single crystal X-ray diffraction data for complexes **1–14** were collected at 100(2) K on a Bruker D8 Venture Duo diffractometer with a Mo X-ray source, $K_{\alpha 1}$ = 0.71073 Å. Adsorption corrections were implemented using the SADABS multi-scan method within the APEX4 software package.[44,45] Structures were solved *via* intrinsic phasing using SHELXT and refined with SHELXL contained within Olex2 1.5.[46–48] All lanthanide, tungsten, and oxygen atoms in the Lindqvist POM complexes were refined anisotropically. While all lattice atoms could be located *via* difference Fourier maps, some of the counter cation and lattice water oxygen atoms were refined with less than full chemical occupancy due to disorder. ISOR restraints were used, when necessary, on lattice oxygen and sodium atoms to produce reasonable thermal ellipsoids. In general, we were able to satisfactorily model disorder throughout complexes **1–14**, except in **4** (NdW_{10}) where there is one lattice Q-peak near a tungsten atom (W2) that could not be dealt with reasonably, and this is the origin of the single Alert A in the CheckCIF report for this complex. This disorder was consistently observed in datasets collected on single crystals from multiple reactions of NdW_{10}, and the data included in the CIF for complex **4** represents the best solution to this structure we were able to obtain. There were not any chemically reasonable ways to model the electron density near W2, thus we have concluded it originates from disorder that is unique to this complex and we have included this information here and in the CheckCIF report submitted to the CCDC. Moreover, hydrogen atoms on the lattice water molecules in all complexes could not be located and thus were not modeled, and these missing hydrogen atoms are the origin of the CheckCIF Alert Bs that are present for all fourteen complexes. All figures for complexes **1–14** were made using CrystalMaker.[49] The crystallographic information for **1–14** can be found in Table S1 (ESI†).

Raman and infrared (IR) spectroscopies. Spectroscopic studies on single crystals of complexes **1–14** involved Raman and attenuated total reflectance infrared (ATR-IR) spectroscopies. Raman spectra for **1–14** were collected on a ReniShaw InVia Raman microscope and for complexes **1–3** (LaW_{10}, CeW_{10}, PrW_{10}), **5–11** (SmW_{10}, EuW_{10}, GdW_{10}, TbW_{10}, DyW_{10}, HoW_{10}, ErW_{10}), **13** (YbW_{10}) and **14** (LuW_{10}) data were collected using a 785 nm laser at varying power, 20× magnification, and the extended scan setting with a range of 1500–100 cm^{-1} with 10 s exposure times and three scans. For complexes **4** (NdW_{10}) and **12** (TmW_{10}), Raman spectra were collected using a 514 nm laser due to fluorescence induced by excitation at 785 nm. Data collection parameters for these two complexes included a range of 1500–100 cm^{-1} with 20× magnification, 30 s exposure times, and six scans. All data collections were conducted in triplicate. Raman data for **1–14** were standardized by dividing raw intensity values by laser power (200 mW, 100% for the 785 nm laser; 1200 mW, 100% for the 514 nm laser) and exposure time. ATR-IR spectra for all complexes were collected in both the mid-IR (MIR) (4500–400 cm^{-1}) and far-IR (FIR) (400–150 cm^{-1}) on a Bruker VERTEX 70v instrument using a platinum ATR microscope objective and the OPUS 8.5 software package. The resolution was 0.4 cm^{-1} for the MIR and 1 cm^{-1} for FIR measurements. IR data collection for all samples were done using half the number of scans used for background scanning ahead of sample measurements. Raman and IR data were baseline corrected using the PreDICT software package and the Origin2023b software package, respectively. The PreDICT software is designed for processing powder X-ray diffraction data; however, there is literature precedent for using the program to process vibrational spectra as well.[50] Peak fitting for both Raman and IR spectra were done with the Origin2023b software package.

Partial least squares (PLS) analysis. PLS combines features of principal component analysis and multiple regression and is designed to produce a predictive model when there are more correlative independent variables than there are dependent variables.[51,52] PLS regression is often used to build predictive models for delineation of multicomponent spectral analysis.[53] In this instance, we are extending the utility of this statistical method to build a model to validate the correlation and predictive ability of structural and distortion parameters for FIR and Raman mode frequencies. PLS regression was done using the singular value decomposition (SVD) method in the Origin2023b software package.[54] The leave-one-out cross-validation protocol was also used to prevent overfitting of the PLS models.[51,52] Structural parameters (skew angle, plane angle, and plane distances) and ionic radii of Ln(III) cations were acquired from either single crystal structure data or the literature,[55] and the structural parameters were then used as

independent variables for PLS analysis with vibrational frequencies used as dependent variables. Each vibrational mode was analyzed independently. More details regarding PLS analysis are provided on pgs. **S59–60** in the ESI.†

Results and discussion

Synthesis

LnW_{10} complexes were first synthesized in 1971 by Peacock and Weakley;[56] however, upon using their protocol we found that our LnW_{10} products also contained a significant amount of sodium paratungstate ($Na_{10}H_2W_{12}O_{40}{\cdot}xH_2O$). In 2020, Mariichak and colleagues published a new procedure for synthesizing LnW_{10} complexes, which we found to consistently yield pure products.[33] The main difference between the two synthesis protocols is that the Peacock and Weakley method uses glacial acetic acid to acidify tungstate solutions whereas the Mariichak protocol employs nitric acid. When characterizing materials made using the Peacock and Weakley method, we found prominent carbonate stretching modes in the MIR spectra of the paratungstate crystals (Fig. S1, ESI†), which suggested that the acetate ions aided in the formation of this byproduct. The use of a strong acid for acidification also enabled the precise addition of stoichiometric quantities of reagents which reduced reaction byproducts. Comparison of the IR spectrum of sodium paratungstate with data from literature did not show agreement between the peak locations;[57] however, we confirmed the identity of this impurity by collecting a single crystal structure X-ray diffraction structure (Fig. S2 and Table S2, ESI†).

Structural description

Single crystal X-ray diffraction analysis revealed that all fourteen LnW_{10} samples are isostructural and crystallize in the $P\bar{1}$ space group. Nine out of fourteen complexes characterized herein are new structures and complexes **1** (LaW_{10}), **3** (PrW_{10}), **5** (SmW_{10}), and **14** (LuW_{10}) are the first Lindqvist POMs with each of these lanthanide cations. Complexes **2** (CeW_{10}), **4** (NdW_{10}), **6** (EuW_{10}), **7** (GdW_{10}), and **8** (TbW_{10}) have known Lindqvist structures; however, we have identified new polymorphs for each of these cations.[27,33–38] Based on crystallographic parameters and packing within unit cells, we identified four distinct polymorphs within the series including complexes **1–3** (LaW_{10}, CeW_{10}, PrW_{10}, polymorph 1), complex **4** (NdW_{10}, polymorph 2), complexes **5–8**, **12**, and **13** (SmW_{10}, EuW_{10}, GdW_{10}, TbW_{10}, TmW_{10}, YbW_{10}, polymorph 3), and complexes **9–11** and **14** (DyW_{10}, HoW_{10}, ErW_{10}, LuW_{10}, polymorph 4). An analysis of unit cell parameters for **1–14** indicated that throughout the four structural polymorphs the length of the crystallographic axes remained consistent with the differences in polymorphs manifesting in changes in α, β, and γ angles. Of the four crystallographic polymorphs identified, polymorphs 1–3 are new additions to the LnW_{10} family, while polymorph 4 is the only structural configuration that has been previously observed.[27,33,34]

The four LnW_{10} polymorphs share many similarities, especially in the metal-ion first coordination sphere, which is consistent throughout complexes **1–14**. As a result, we will only describe the metal-ion local coordination for complex **10** (HoW_{10}), which is representative of the whole Ln-Lindqvist series. Complex **10** features a single crystallographically unique eight coordinate Ho(III) metal center that has adopted slightly distorted square antiprismatic (D_{4d}) molecular geometry. The Ho(III) ion in **10** is sandwiched by two crystallographically unique $[W_5O_{18}]^{6-}$ (W_5) lacunary POMs that are each comprised of five edge-sharing WO_6 octahedra. Four oxygen atoms from each W_5 moiety bind to the Ho(III) metal center, and collectively the Ho(III) ion and the two W_5 lacunary POMs can be described as a HoW_{10} POM cluster. The average Ho–O bond distance in **10** is 2.366 Å, and in the LnW_{10} series the average Ln–O bond distances (d_{Ln-O}) range from 2.5194 Å (for La(III) – complex **1**) to 2.337 Å (for Lu(III) – complex **14**).

POM coordination to the Ho(III) cation in **10** generated two inequivalent WO_6 units in each W_5 moiety (WO_6 cap and WO_6 belt) (Fig. S3, ESI†). Within the coordinating WO_6 belt, we identified five distinct W–O bonds, W–$O_{lanthanide}$, W–O_{center}, W–O_{bridge}, W–$O_{terminal}$, and W–O_{cap}, and a detailed schematic highlighting each of these can be found in Fig. S3 (ESI†). In complex **10**, the average W–$O_{lanthanide}$ distance is 1.793 Å with a range of 1.787–1.799 Å. The average W–O_{center} bond distance is 2.316 Å with a range of 2.289–2.373 Å, while W–O_{belt} distances are shorter at an average of 1.949 Å with a range of 1.930–1.969 Å. For W–$O_{terminal}$ bonds, the average distance is 1.735 Å with a range of 1.726–1.740 Å and W–O_{cap} bonds are at an average distance of 2.020 Å with a range of 2.004–2.040 Å. The WO_6 cap moieties are at the apex of each W_5 cluster and are not involved in lanthanide coordination. These structural units feature only three unique W–O bonds, W–O_{center}, W–$O_{terminal}$, and W–O_{belt}, and in HoW_{10}, the W–O_{center} and W–$O_{terminal}$ bonds are at an average of 2.252 Å and 1.744 Å, respectively, while the W–O_{belt} bonds are at an average of 1.910 Å with a range of 1.879–1.952 Å. Overall, there are no observable correlations between changes in Ln(III) ionic radii and the different W–O bond distances, and the values exhibited by complex **10** are typical for the entire series. Beyond the first coordination sphere in **10**, there is a network of nine Na(I) cations for charge balancing and 35 lattice water molecules. The varying configurations of water and Na(I) cations in the second coordination sphere are what differentiate the four polymorphs within the LnW_{10} series.

For polymorph 1, the nine Na(I) cations are distributed between two fragments on the periphery of the cluster (Fig. 1a). One fragment contains six sodium cations while the other contains three sodium cations, and the closest distances between Ln(III) and Na(I) (d_{Ln-Na}) cations are 5.547 Å, 4.211 Å, and 4.197 Å for complexes **1–3** (LaW_{10}, CeW_{10}, PrW_{10}), respectively. Sodium cations in the lattices of complexes **1–14** generally feature octahedral coordination (NaO_6) environments except for the Na(I) cation closest to the Ln(III) metal centers in complexes **2** and **3**, which exhibits tetrahedral geometry. Complex **1** is also distinct amongst polymorph one species

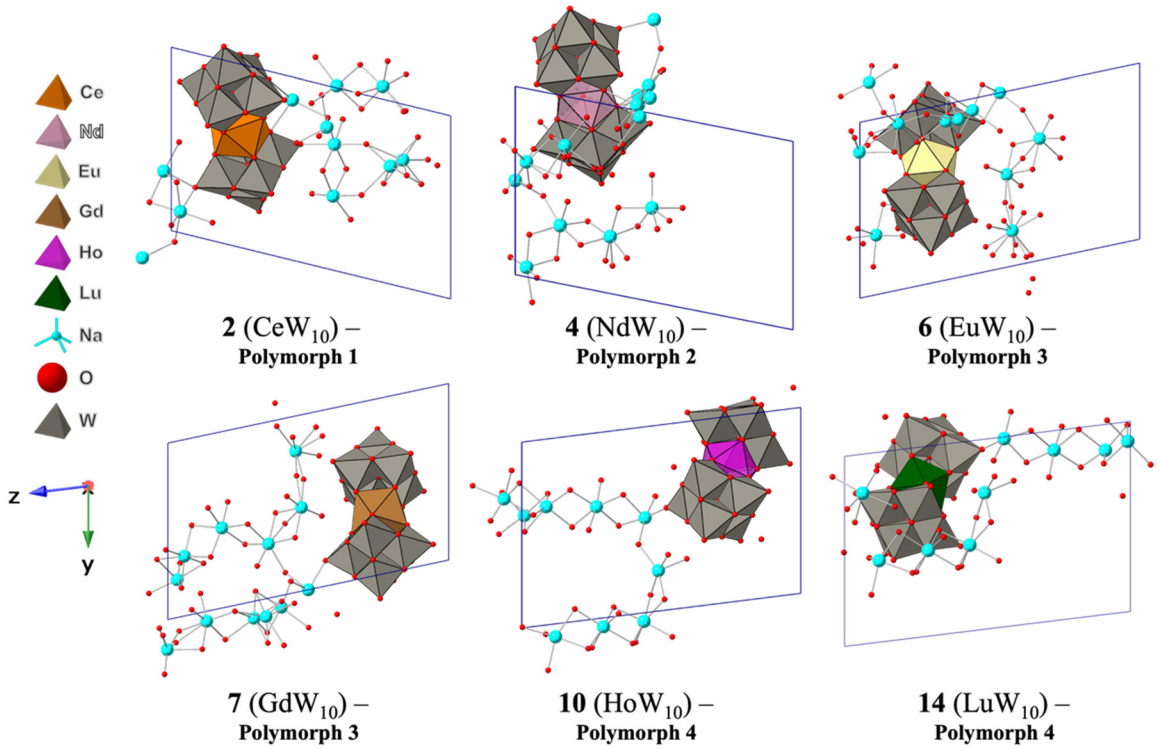

Fig. 1 Polyhedral models in the (100) plane of the asymmetric units for complexes **2**, **4**, **6**, **7**, **10**, and **14** that show the different configurations of NaO_6 units within each polymorph. Complex **2** is a representative example for polymorph one species, complex **4** is the only example of polymorph 2, complexes **6** and **7** are representative examples of the two NaO_6 configurations found in polymorph three structures, and complexes **10** and **14** are representative examples for polymorph four.

since instead of having Na(I) in this tetrahedral hole, it has a water molecule, Fig. S5 (ESI†). The number of lattice waters for complexes **1–3** are 34, 28, and 29, respectively, and it is important to note that the variance in the number of lattice water molecules may originate from the disorder of the crystal structures since the crystals readily desolvate under ambient conditions. For polymorph 2 (complex **4**), the nine NaO_6 moieties form a helix pattern around the cluster, Fig. 1b, with a closest d_{Ln-Na} of 4.436 Å. The number of lattice water molecules in **4** (NdW_{10}) is 32 and notably they are packed tightly in a helical pattern resulting in a much smaller unit cell (V = 3070 Å^3) compared to polymorphs 1, 3, and 4 (V = ~3250 Å^3). The close packing of polymorph 2 resulted in four partial clusters included in each unit cell instead of the two partial clusters included in unit cells for the other polymorphs, Fig. S6 (ESI†). This compactness is also reflected in closest distances between Ln(III) cations (d_{Ln-Ln}) which is 9.987 Å for polymorph 2, while for polymorphs 1, 3, and 4 d_{Ln-Ln} values range from 11.153 Å to 11.537 Å. Inspection of the asymmetric unit in polymorph 3 revealed two configurations of the NaO_6 fragments, Fig. 1c and d. Complexes **5**, **7**, and **13** (SmW_{10}, GdW_{10}, YbW_{10}) feature all nine NaO_6 moieties connected to form a single fragment contained above the clusters for **5** and **13** and to the side of the cluster for **7**. For complexes **6**, **8**, and **12** (EuW_{10}, TbW_{10}, TmW_{10}) the nine NaO_6 moieties form two fragments of seven and two Na(I) units that are located on the periphery of the clusters. For complexes **5–8**, **12**, and **13**, the closest d_{Ln-Na} are 5.672 Å, 5.645 Å, 5.710 Å, 5.705 Å, 5.635 Å, and 5.716 Å, respectively, and complexes **5–7** include 36 lattice water molecules, while complexes **8**, **12**, and **13** feature 37, 35, and 37 lattice waters, respectively. Similar to polymorph 3, there is variance in NaO_6 configurations in the structures of polymorph 4 complexes, Fig. 1e and f. For example, complexes **9** and **10** (DyW_{10}, HoW_{10}) feature nine NaO_6 moieties connected to form a single fragment that adopts a fork-like pattern, whereas complexes **11** and **14** (ErW_{10}, LuW_{10}) include NaO_6 units that are split into two fragments, analogous to the packing seen in polymorph 1. The closest d_{Ln-Na} for **9**, **10**, **11**, and **14** are 5.456 Å, 5.446 Å, 5.292 Å, and 5.446 Å, respectively, and complexes **9–11** include 35 lattice water molecules, while complex **14** has 32. These d_{Ln-Na} interaction distances and lattice compositions are consistent with literature data for polymorph 4 structures.[27,33,34]

The differences between polymorphs 1–4 can also be seen by analyzing the patterns produced by the Na(I) cations in the unit cell when each is viewed in the same orientation, Fig. 2. Inspection of complexes that adopt the polymorph 1 configuration reveals a consistent zigzag pattern with the Ln(III) cations located within the packing motif as highlighted in Fig. 2a. The pattern produced by the Na(I) cations in complex **4** (polymorph 2) is the most complicated in the series and is best described as a mix of zigzag and hourglass patterns with a line bisecting

the packing schemes, Fig. 2b. The location of the Nd(III) cations is also unique compared to the other polymorphs as they are located on the faces of the unit cell. In polymorph 3, complexes **5–8** (SmW_{10}, EuW_{10}, GdW_{10}, TbW_{10}) exhibit a mix of zigzag and hourglass patterns for the Na(I) cations with the Ln(III) cations located inside the pattern, Fig. 2c, while complexes **12** and **13** (TmW_{10}, YbW_{10}) feature Na(I) cations in an hourglass pattern with the Ln(III) cations located outside the pattern, Fig. 2e. Finally, for complexes **9–11** and **14** (DyW_{10}, HoW_{10}, ErW_{10}, LuW_{10}, polymorph 4) the Na(I) cations form a whirlpool pattern with the Ln(III) cations integrated into the packing motif, Fig. 2d.

Structural discussion

Synthesizing Lindqvist POM complexes with all fourteen lanthanides enabled us to probe the extent of distortion away from ideal D_{4d} symmetry for each Ln(III) cation. This is relevant for understanding the clock transition in HoW_{10} and for ascertaining the design principles that may allow for similar transitions to be accessed in other complexes featuring the same metal-ion point group symmetry. To obtain distortion information we focused on three parameters that are characteristic of each lanthanide Lindqvist POM: the skew angle (SA), the coordination plane angle (PA), and the coordination plane distance (PD). These values can be determined based on crystal structures alone and have been identified by Coronado and colleagues as key parameters for tuning crystal field splitting within lanthanide POM complexes.[40,58] The SA represents the angle, φ, produced by rotation of one of the coordinating planes with respect to the other coordinating plane, and in ideal D_{4d} symmetry the skew angle is 45°. Of note, there is not a standard method for determining SA values and our skew angle data for **10** (HoW_{10}) and **11** (ErW_{10}) deviates from previously published data from Coronado *et al.*,[58] which is likely due to different methods used to determine these values, and more detail about our methodology for calculating SA values can be found in Fig. S4 (ESI†). Our rationale for developing an updated method for determining skew angles is to ensure reproducibility across our work and other studies going forward. The PA is the angle between the two coordinating planes and in ideal D_{4d} symmetry this value would be 0° due to the two planes lying parallel to one another. PDs provide information on the proximity between the two coordinating planes and for ideal D_{4d} symmetry this distance would be 0 Å. Details regarding our methodologies for obtaining PD and PA values for complexes **1–14** can also be found in Fig. S4 (ESI†).

Once distortion parameters were obtained for complexes **1–14**, we investigated whether any changes could be correlated to the identity of the Ln(III) cation. This was initially done by comparing SA, PA, and PD values with ionic radii of the Ln(III) cations, and these plots are shown in Fig. 3. There are no general trends observed in comparisons of distortion parameters with the entire lanthanide series; however, when we grouped the different LnW_{10} complexes by structural polymorph, we did note polymorph specific trends for each of structural distortion parameters. These results are presented

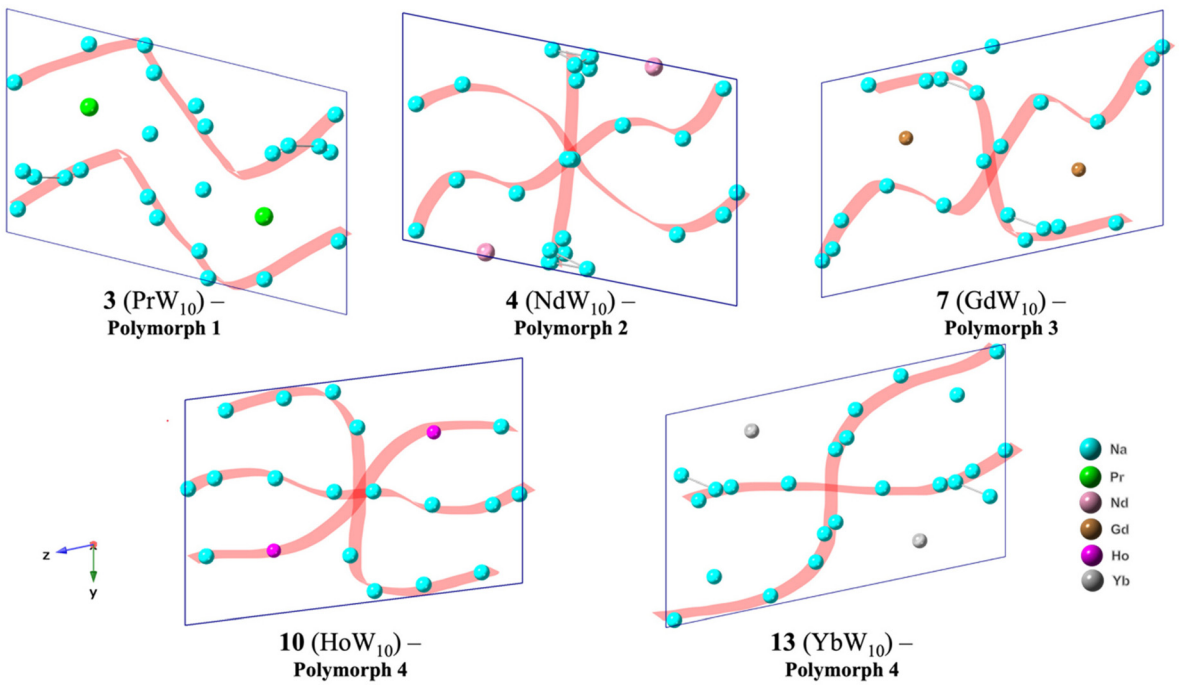

Fig. 2 Models in the (100) plane displaying the unit cell contents of complexes **3**, **4**, **7**, **10**, and **13**, which highlight the unique patterns formed by the Na(I) cations that allow for differentiation between polymorphs. Complex **3** is representative example for polymorph 1, complex **4** is the only example of polymorph 2, complexes **7** and **13** display the two patterns observed in polymorph three structures, and complex **10** is a representative example for polymorph four species. Oxygen and tungsten atoms were omitted for clarity.

in Fig. 3 and S7–S9 (ESI†) and based on these plots we can identify some of the characteristics that make HoW_{10} unique within the LnW_{10} series. The skew angles of polymorph 1 (complexes **1–3**) range from 3.34° (**3**, PrW_{10}) to 3.77° (**1**, LaW_{10}) and within this group of complexes the decrease in skew angle corresponds to the decrease in ionic radii from La(III) to Pr(III) (Fig. 3 and Fig. S7, ESI†). Polymorph 2 (complex **4**) has a skew angle of 6.25° that is significantly higher than what we observed for any of the other polymorphs (Fig. 3), and since this configuration is only adopted by one complex it limits what we can learn about this structure. The skew angles for polymorph three complexes (**5–8**, **12**, and **13**) decrease as lanthanide ions get smaller, consistent with polymorph one, and range from 3.98° (**12**, TmW_{10}) to 4.20° (**5**, SmW_{10}) (Fig. 3 and Fig. S7, ESI†). For polymorph 4 (complexes **9–11** and **14**), the skew angles increase as the ionic radii decreases; however, there is an outlier to this trend in complex **11** (ErW_{10}) which exhibits a much smaller skew angle of 1.94°. The remainder of polymorph 4 complexes have skew angles ranging from 2.09° (**9**, DyW_{10}) to 2.12° (**14**, LuW_{10}) (Fig. 3 and Fig. S7, ESI†), and it is the polymorph 4 configuration that is notable as these structures features the smallest skew angles amongst LnW_{10} complexes.

PA values for polymorph 1 complexes display a similar correlation to Ln(III) ionic radii as what was observed for SAs, specifically, there is a decrease in plane angle as metal ions get smaller with PA values ranging from 2.71° (**3**, PrW_{10}) to 4.81° (**1**, LaW_{10}) (Fig. 3 and Fig. S8, ESI†). For polymorph 2, the plane angle is 2.31° which falls within the range of PA values observed for other LnW_{10} polymorphs. PA values for polymorph 3 complexes also follow the established trend of decreasing as the lanthanide ionic radii decreases with values ranging from 1.89° (**12**, TmW_{10}) to 2.35° (**5**, SmW_{10} and **6**, EuW_{10}) (Fig. 3 and Fig. S8, ESI†). Plane angles for polymorph 4 complexes also decrease as lanthanide ions get smaller with values ranging from 1.14° (**14**, LuW_{10}) to 1.17° (**9**, DyW_{10}); however, there is an outlier to this trend, which is complex **10** (HoW_{10}), that has a plane angle of 1.13° (Fig. 3 and Fig. S8, ESI†). Comparing the PAs across the series, we note that polymorph 4 complexes feature the smallest plane angles, whereas polymorph 1 complexes have the largest plane angles. The plane distances for the polymorph 1 structures range from 0.003 Å to 0.023 Å (Fig. 3 and Fig. S9, ESI†). Similar to SA and PA values for polymorph 1 complexes, there is a decrease in plane distances as the Ln(III) ionic radii shrink. For polymorph 2, the plane distance (**4**, NdW_{10}) is in line with other polymorphs and the PD value for this complex is 0.011 Å. The plane distances for polymorph 3 complexes have a uniform spread that ranges from 0.013 Å (**7**, GdW_{10}) to 0.019 Å (**6**,

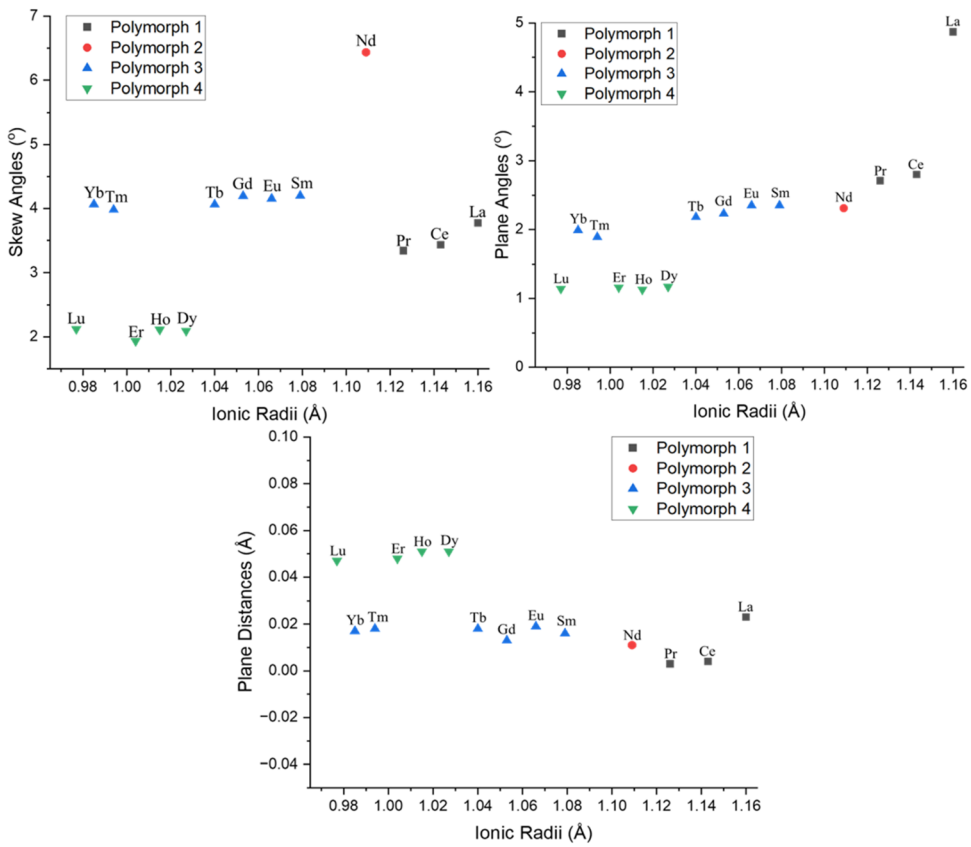

Fig. 3 Plot of structural distortion parameters of complexes **1–14** *versus* lanthanide ionic radii. (Top left) Skew angle *vs.* ionic radii. (Top right) Plane distance *vs.* ionic radii. (Bottom) Plane angle *vs.* ionic radii. These plots show that there are clear groupings of distortion parameter values based on the polymorphs adopted by the LnW_{10} complexes.

EuW_{10}) (Fig. 3 and Fig. S9, ESI†). Moreover, the PD values for polymorph 4 structures decrease as the metal ion ionic radii decreases, similar to the trend noted above for polymorph 1, with values ranging from 0.047 Å (**14**, LuW_{10}) to 0.051 Å (**10**, HoW_{10}) (Fig. 3 and Fig. S9, ESI†). Comparing the different polymorphs in the series, polymorph 4 exhibits the longest plane distances amongst the four polymorphs, while polymorphs 1–3 display relatively similar plane distances.

Overall, the polymorph specific trends in structural distortion parameters that were identified for complexes **1–14** indicate that the composition and packing of the lattice plays a major role in modulating the effective symmetry and tuning the crystal field of the Ln(III) metal centers. Comparisons of d_{Ln-Na} interaction distances *versus* ionic radii of the Ln(III) cations also reveals polymorph based correlations which further strengthens this observation, Fig. S10 (ESI†). In HoW_{10}, the M_J = ±4 ground state was stabilized and further mixed by the distorted D_{4d} symmetry, which facilitates the atomic clock transition that has been observed in this complex.[24] Due to selection rules, tunneling between M_J states is forbidden in Kramers ions (J = non-integer), hence clock transitions can only exist in non-Kramers ions (J = integer).[24,25,59] In the Ln(III) series, this includes Pr(III), Pm(III), Eu(III), Tb(III), Ho(III), and Tm(III). It has been hypothesized that the clock transition of the HoW_{10} complex could be re-created if the effective symmetry around the Ho(III) cation was emulated in the other non-Kramers LnW_{10} species.[16,60] Herein we have shown that the distortion parameters for HoW_{10} (complex **10**) are distinct from Lindqvist POM complexes with the other non-Kramers Ln(III) cations, and this provides a potential explanation for why only the HoW_{10} complex has displayed an accessible atomic clock transition. To re-create the effective symmetry of the HoW_{10} complex in other LnW_{10} species, alternative means for controlling structural distortion parameters and second coordination sphere packing will be necessary, and pathways for pursuing this aim include novel crystallization methods and inclusion of different charge balancing cations.[27]

Vibrational spectroscopy results

According to the normal mode analysis conducted by Kazanskii *et al.*,[61] there should be a total of 76 vibrational bands for a LnW_{10} complex with D_{4d} symmetry. The vibrations are categorized as Γ = 13 A_1 (Raman active) + 13 B_2 (IR active) + 18 E_1 (IR) + 15 E_2 (Raman) + 17 E_3 (Raman); however, the number of bands observed in Raman and IR spectra can vary because these calculations are done assuming ideal symmetry that does not account for the coupling of modes with lattice vibrations. Mid-IR (MIR), far-IR (FIR), and Raman spectra for complexes **1–14** were collected and data fitting and vibrational mode assignments were completed based on previous literature results.[31,34,41,61] Since improving understanding of spin-phonon coupling within f-element POMs was the primary focus of our vibrational spectroscopy efforts, we focused on the low energy region (400–100 cm^{-1}) where peaks associated with spin-phonon coupling are generally observed in infrared and Raman spectra. Notably, in contrast to structural results for complexes **1–14**, there are no polymorph specific differences in the vibrational spectra, thus we use representative examples in this section to describe the vibrational characteristics of the series in detail.

Data collection and peak identification in FIR spectra is challenging due to signals that are overwhelmed by water absorption effects and possible mode couplings between cluster and lattice elements that can result in jagged and broad features instead of well-defined peaks. To identify FIR features for complexes **1–14**, spectra were fitted with Gaussian peak profiles and the FIR spectrum of HoW_{10} (complex **10**) was used as a representative example for the entire series. Peak assignments were made based on the calculations from Blockmon and colleagues who conducted a far-IR magnetospectroscopy study on HoW_{10} that included eight peaks in the spectral window of 400–100 cm^{-1}.[31] Interestingly, we only observed six peaks in the same spectral window after background subtraction (Fig. 4), and this may be due to our instrument not being able to resolve the complex vibrational features present in this region. The six peaks identified for **10** in the FIR are centered at 357 cm^{-1}, 319 cm^{-1}, 200 cm^{-1}, 175 cm^{-1}, 146 cm^{-1}, and 120 cm^{-1}. The peak at 354 cm^{-1} was assigned as a $\rho/\delta(HoO_4)$ (ν = stretching, δ = bending) mode and the peak at 319 cm^{-1} was assigned as a $\nu/\rho(HoO_8)$ (ρ = rocking) mode. The peak at 200 cm^{-1} was assigned to the $\rho(W_5O_{18})$ mode; however, this peak only shows up in spectra for complexes **9** and **10** (DyW_{10}, HoW_{10}), and since there are no structural features that are unique to complexes **9–10**, we suspect this peak is present for all complexes and only observable for these two complexes. The two final peaks at 175 cm^{-1} and 146 cm^{-1} were assigned as $\rho(HoO_8)$ and $\nu(WO_5)_2$ modes, respectively. The peak at 120 cm^{-1} does not match with any known stretches for this Ln POM system, yet spectra collected by

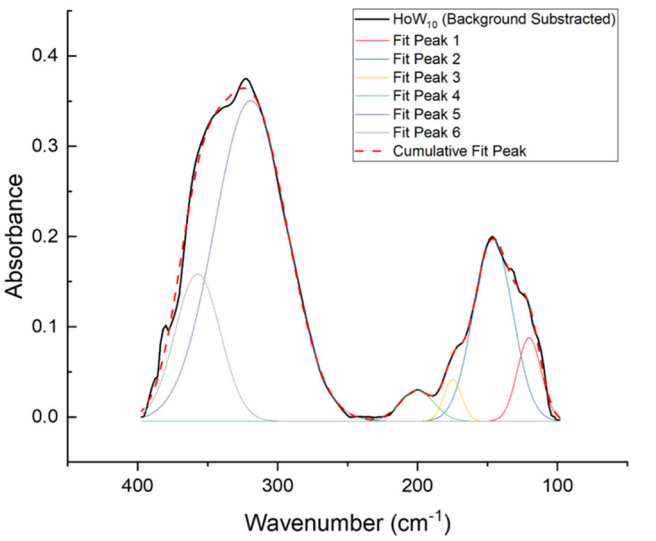

Fig. 4 Background subtracted FIR spectrum (400–100 cm^{-1}) for complex **10** (HoW_{10}) fit to Gaussian functions.

Blockmon and colleagues show an unidentified peak at 113.4 cm^{-1}, which may correspond to the peak we observe for **10**.[31] Raw and fitted FIR spectra for complexes **1–14** (Fig. S11–24, ESI†) as well as tables listing the peaks and peak fitting parameters for each FIR spectra (Tables S3–S17, ESI) are available in the ESI.†

Raman spectra were collected for complexes **1–14** and peak identification and data fitting was based on the assignments made by Shiozaki *et al.* and Kazanskii and colleagues.[41,61] The Raman spectrum of HoW_{10} (complex **10**) was used as a representative example, and the fitted Raman spectrum for **10** using Lorentzian peak profiles is presented in Fig. 5, which includes twelve major peaks in the spectral window of interest (1020–100 cm^{-1}). The sharp peaks at 952 cm^{-1} and 935 cm^{-1} were assigned as $\nu(W{=}O_t)$ modes, while the peak at 888 cm^{-1} was assigned to the ν(Ln–O–W) mode. The peaks centered at 834 cm^{-1} and 554 cm^{-1} were assigned as ν(W–O–W) modes. At lower energies, the peaks at 428 cm^{-1} and 360 cm^{-1} were identified as the δ(W–O–W/W═O/Ln–O–W) mode, and the remaining peaks at 326 cm^{-1}, 214 cm^{-1}, 171 cm^{-1}, and 137 cm^{-1} were attributed to deformation modes of the HoW_{10} POM. We also observed a significant change in select peak intensities when the orientation of the sample was changed during measurements. This implies that some of these vibrational modes are polarizable which is a characteristic sign that the vibrational modes are likely part of the A_1 irreducible representation.[62] More specifically, we noted that the 888 cm^{-1} peak, which is assigned as the ν(Ln–O–W) mode, fluctuates in intensity when different crystals of the same sample are measured (Fig. S25, ESI†). Interestingly, according to the literature this band is not supposed to be polarizable,[61] and thus changes in peak intensity as a function of crystal orientation are unexpected. Moreover, we also found features in the 200 cm^{-1} region that fluctuate in similar manner, which is in agreement with previous observations from Kazanskii *et al.*[61] Raw and fitted Raman spectra along with a table listing peaks observed in complexes **1–14** are available in the ESI (Fig. S26–S39, Tables S18–S32, ESI†), and overall, comparisons of the spectra for **1–14** show good agreement with the results from Shiozaki *et al.* and Kazanskii and colleagues wherein eight to twelve features are observed in the 1020–100 cm^{-1} spectral window with comparable peak locations.[41,61]

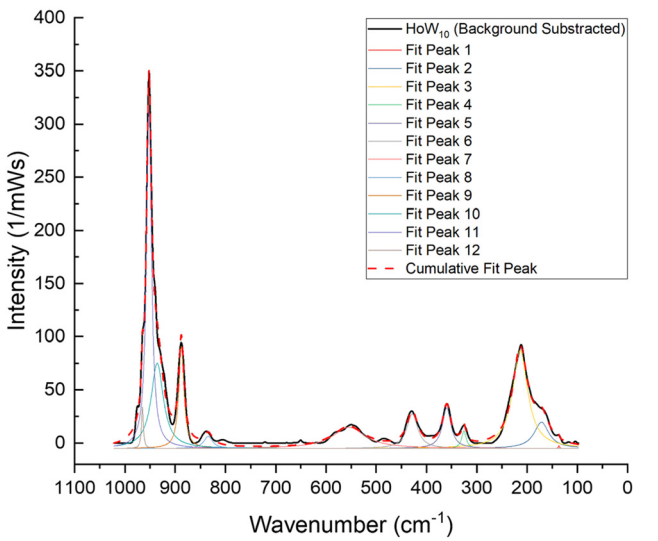

Fig. 5 Background subtracted Raman spectrum for complex **10** (HoW_{10}) fit to Lorentzian functions.

The MIR spectrum of ErW_{10} (complex **11**) will be discussed in detail since this allowed for matching our spectrum assignments to those made by Radio *et al.* in their study on GdW_{10} and ErW_{10} complexes.[34] Comparing the overall features of the MIR spectrum of **11** with literature results, we found that vibrational bands in our spectrum were consistently redshifted by approximately 10 cm^{-1} which may be due to our use of an Attenuated Total Reflectance (ATR) probe rather than the more traditional KBr pellet.[63] The MIR features centered at 3353 cm^{-1}, 1650 cm^{-1}, and 1635 cm^{-1} were assigned to ν(O–H) and δ(H–O–H) stretches of water. The broad peak at 1357 cm^{-1} and the sharp peak at 968 cm^{-1} were assigned to the $\nu_{as}(NO_3)$ and $\nu(NO_3)$ modes of $NaNO_3$, respectively. The presence of $NaNO_3$ is expected as it is the main byproduct in our synthetic process. The peak at 921 cm^{-1} corresponds to the $\nu(W{=}O_t)$ mode, while peaks at 833 cm^{-1}, 777 cm^{-1}, 694 cm^{-1}, 582 cm^{-1}, 538 cm^{-1}, and 480 cm^{-1} were assigned as ν(W–O–W) modes. The final peak at 405 cm^{-1} was assigned as the δ(W–O–W) mode. Overall, there is a good agreement between the MIR spectrum of **11** and the results from Radio and colleagues in terms of peak locations.[34] Peak fitting was also conducted on the MIR spectrum of 11 from 1200–400 cm^{-1} and the fitted spectrum and fit details can be found in Fig. S40 and Table S33 (ESI†).

Structure vibrational property relationships

Elucidating structure–vibrational property relationships in Ln Lindqvist POMs is critical for understanding how to limit spin-phonon coupling processes that can lead to decoherence. A holistic approach to understanding how changes in first coordination sphere bonding and second coordination sphere packing impact vibronic coupling necessitates comprehensive experimental studies that are paired with DFT and CASSCF calculations. While the latter areas are beyond our expertise and outside the scope of this study, we were able to initiate the process of delineating structure–vibrational property relationships for LnW_{10} complexes by selecting major vibrational peaks from the FIR and Raman spectra that were consistently observed and looking for trends as a function of the structural features within complexes **1–14**. From the FIR region, three peaks centered at 146 cm^{-1}, 175 cm^{-1}, and 319 cm^{-1} fit these criteria which correspond to the $\nu(WO_5)_2$, $\rho(LnO_8)$, and ν/$\rho(LnO_8)$ modes, respectively. The peaks were plotted against structural parameters and data from triplicate measurements were averaged before inclusion in final plots.

The plot of frequencies of the $\nu(WO_5)_2$ mode *versus* the ionic radii of the Ln(III) cations is presented in Fig. 6, which shows a general decrease in the frequency of $\nu(WO_5)_2$ modes

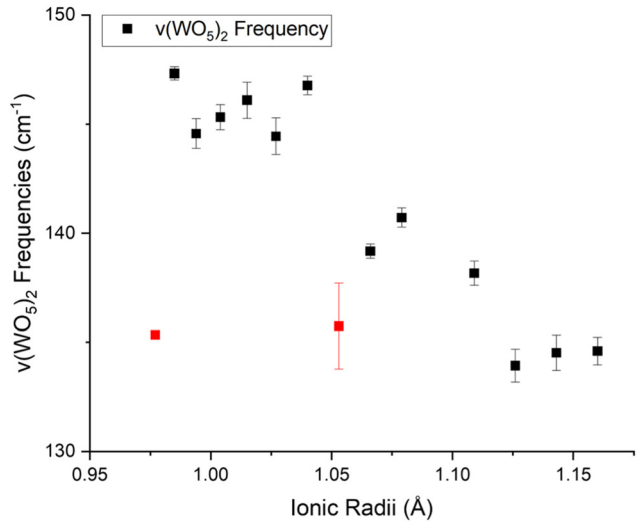

Fig. 6 Plot of FIR $\nu(WO_5)_2$ frequencies *versus* lanthanide ionic radii for complexes **1–14**. Red data-points (complexes **7** and **14**) are outliers in the series (see discussion). Error bars represent uncertainties of the peak center obtained from the fitting regime.

as we move to larger Ln(III) cations with two clear outliers in complexes **7** and **14** (GdW_{10} and LuW_{10}). We evaluated the W–O bond distances of the coordinating WO_6 unit in complexes **7** and **14** to see if this was the origin of the anomalous behavior; however, these values were consistent with W–O distances throughout the LnW_{10} series. We also compared structural distortion parameters of **1–14** with $\nu(WO_5)_2$ mode frequencies, which show correlations between the FIR mode and SA, PA, and PD values when complexes of the same polymorph are compared. A look at the relationship between the frequencies of $\nu(WO_5)_2$ modes and SAs shows that there is a blueshift in mode frequency as the SA grow larger for polymorph 1 structures, whereas the trend is flipped for polymorph 3 and 4 complexes (Fig. S41, ESI†) and $\nu(WO_5)_2$ mode frequencies redshift as SAs increase (Fig. S41, ESI†). In the comparison of $\nu(WO_5)$ frequencies *versus* PAs, polymorph 1 structures exhibit a blueshift in the stretching mode as PAs increase, while polymorph 3 complexes do not display any type of correlation (Fig. S42, ESI†). Similar to what was observed in the comparison with SA values, $\nu(WO_5)_2$ mode frequencies for polymorph 4 structures redshift as PAs increase with an outlier in complex **14** (Fig. S42, ESI†). In comparisons with metal complex PDs, polymorph 1 structures once again feature a redshift in $\nu(WO_5)_2$ stretching frequencies as PDs increase, while polymorph 3 complexes do not display any type of clear correlation, consistent with SA and PA results described above (Fig. S43, ESI†). Interestingly, $\nu(WO_5)_2$ mode frequencies for polymorph 4 structures blueshift as PDs increase, which is a change from the trends observed for SA and PA values (Fig. S43, ESI†). In general, structural distortion parameters consistently show correlations with the $\nu(WO_5)_2$ mode frequencies in polymorph 1 and 4 structures, whereas no relationship between the stretching mode and polymorph 3 structural parameters is observed. This suggests that distortion parameter effects on the $\nu(WO_5)_2$ frequency are distinct for each LnW_{10} polymorph, which indicates that secondary interactions with lattice elements play a role in tuning this FIR vibrational band.

Changes in $\rho(LnO_8)$ frequencies were compared with lanthanide ionic radii and the results are presented in Fig. 7, which shows that the frequency of this FIR spectral band blueshifts as the ionic radii of the metal center increases, except for one outlier peak corresponding to complex **7** (GdW_{10}). It is important to note that we did not identify a peak suitable for this mode for complex **14** (LuW_{10}), thus it is not included in this analysis. We also compared $\rho(LnO_8)$ mode frequencies with structural distortion parameters of **1–14** to gain insights into possible polymorph-based correlations and found trends in how this FIR mode shifted as a function of SA, PD, and PA values when complexes of the same polymorph are compared. A look at the relationship between the frequencies of $\rho(LnO_8)$ modes and SAs shows that for polymorph 1 and 3 complexes the mode blueshifts as SAs increase, while for polymorph 4 structures no trends were observed (Fig. S44, ESI†). In comparisons with metal complex PAs, $\rho(LnO_8)$ frequencies for polymorph 1 and 3 complexes were also found to blueshift with increasing PA values (Fig. S45, ESI†). In contrast, $\rho(LnO_8)$ modes for polymorph 4 structures redshifted in frequency with larger PA values (Fig. S45, ESI†). In the comparison of $\rho(LnO_8)$ frequencies *versus* PDs, similar trends to those observed with SAs were noted with polymorph 1 and 3 complexes featuring $\rho(LnO_8)$ modes that blueshift when PDs increase, whereas for polymorph 4 structures no correlations between the two parameters were identified (Fig. S46, ESI†). In general, structural distortion parameters consistently show correlations with the $\rho(LnO_8)$ mode frequencies in polymorph 1 and 3 structures, while no relationship between the stretch-

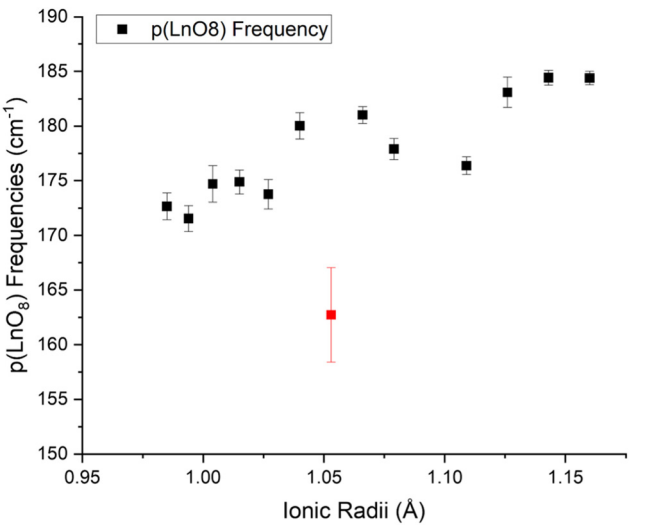

Fig. 7 Plot of FIR $\rho(LnO_8)$ frequencies *versus* lanthanide ionic radii for complexes **1–14**. Red data-point (complex **7**) is an outlier to the trend (see discussion). Error bars represent uncertainties of the peak center obtained from the fitting regime.

ing mode and polymorph 4 structural parameters is observed except for with PA values. These findings support the takeaway from $\nu(WO_5)_2$ frequency *versus* distortion parameter comparisons, specifically that secondary interactions with lattice elements are capable providing a route to tune FIR vibrational modes.

For the frequencies of the $\nu/\rho(LnO_8)$ mode, a redshift is observed as we move to larger Ln(III) cations except for complex **1** (LaW_{10}) which is a likely outlier (Fig. 8). Consistent with trends observed for other FIR modes, plotting $\nu/\rho(LnO_8)$ frequencies *versus* structural distortion parameters highlights polymorph based trends. When comparing $\nu/\rho(LnO_8)$ mode frequencies with SAs, there is noticeable blueshift as SA values increase for polymorph 1 structures, while polymorph 3 and 4 complexes display the opposite behavior with mode frequencies redshifting as SAs increase (Fig. S47, ESI†). Comparisons of $\nu/\rho(LnO_8)$ mode frequency *versus* PA values yield similar trends to those observed with SAs for polymorph 1 and 3 complexes, whereas for polymorph 4 structures no correlations are observed (Fig. S48, ESI†). The relationship between $\nu/\rho(LnO_8)$ mode frequencies and PDs for complexes **1–14** is the most varied with polymorph 1 structures consistently displaying a blueshift in vibrational frequency with increasing PD values (Fig. S49, ESI†). For polymorph 3 complexes, we note two trends: complexes **6**, **8**, **12**, and **13** (EuW_{10}, TbW_{10}, TmW_{10}, YbW_{10}) show the $\nu/\rho(LnO_8)$ mode redshifting as the PD increases, while complexes **5** and **7** (SmW_{10}, GdW_{10}) display the opposite relationship (Fig. S49, ESI†). For polymorph 4 structures, the frequency of the $\nu/p(LnO_8)$ mode redshifts as PDs increase, in a similar manner to how $\nu/p(LnO_8)$ frequencies evolved as function of SAs for this same group of complexes (Fig. S49, ESI†).

In the Raman spectra of **1–14**, two peaks centered at 360 cm^{-1} and 888 cm^{-1}, corresponding to the [δ(W–O–W/W═O/Ln–O–W)] and [ν(Ln–O–W)] modes, respectively, were chosen to be analyzed in further detail. The frequencies of both Raman modes were compared against lanthanide ionic radii and the results are presented in Fig. 9 and 10. A blueshift in the δ(W–O–W/W═O/Ln–O–W) frequencies can be observed as Ln(III) cations increase in size. On the other hand, we observed a redshift in ν(Ln–O–W) frequencies as Ln(III) cations increase in size; however, there is variance in this trend as complexes **7–10** and **12** (GdW_{10}, TbW_{10}, DyW_{10}, HoW_{10}, TmW_{10}) do not follow the linear decrease in frequency that is characteristic of early and late LnW_{10} complexes.

Comparing Raman mode frequencies against structural distortion parameters did not yield any correlations for the [δ(W–O–W/W═O/Ln–O–W)] mode (Fig. S50–52, ESI†), whereas plots of ν(Ln–O–W) frequencies *versus* SA, PA, and PD values revealed polymorph based correlations, consistent with FIR results described earlier (Fig. S53–55, ESI†). We found that ν(Ln–O–W) mode frequencies for polymorph 1 and 4 complexes redshift as SAs increase, while for polymorph 3 structures there was not any relationship between the two parameters (Fig. S53, ESI†). The analogous comparisons of ν(Ln–O–W) modes *versus* PAs show that polymorph 1 complexes feature redshifts in Raman frequencies as PA values increase, whereas there are not any trends for polymorph 3 and 4 structures (Fig. S54, ESI†). In the plot of ν(Ln–O–W) frequencies *versus* PDs, we observed that Raman modes redshift for polymorph 1 and 4 complexes as PDs increase, while for polymorph 3 structures the opposite trend is exhibited with ν(Ln–O–W) frequencies blueshifting with larger PD values (Fig. S55, ESI†). The correlations noted in Fig. 9 and the absence of similar phenomena in comparisons with structural distortion parameters for the δ(W–O–W/W═O/Ln–O–W) Raman mode implies that this band is only influenced by the interaction between the Ln(III) center and the coordinating oxygen atoms.

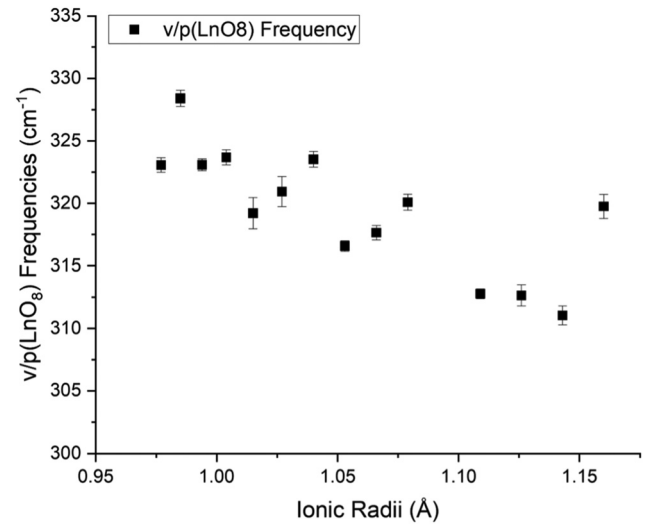

Fig. 8 Plot of FIR $\nu/\rho(LnO_8)$ frequencies *versus* lanthanide ionic radii for complexes **1–14**. Error bars represent uncertainties of the peak center obtained from the fitting regime.

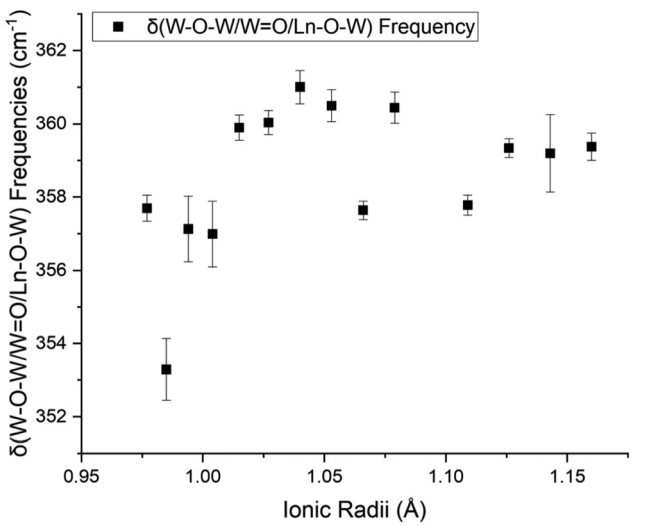

Fig. 9 Plot of Raman δ(W–O–W/W═O/Ln–O–W) frequencies *versus* lanthanide ionic radii for complexes **1–14**. Error bars represent uncertainties of the peak center obtained from the fitting regime.

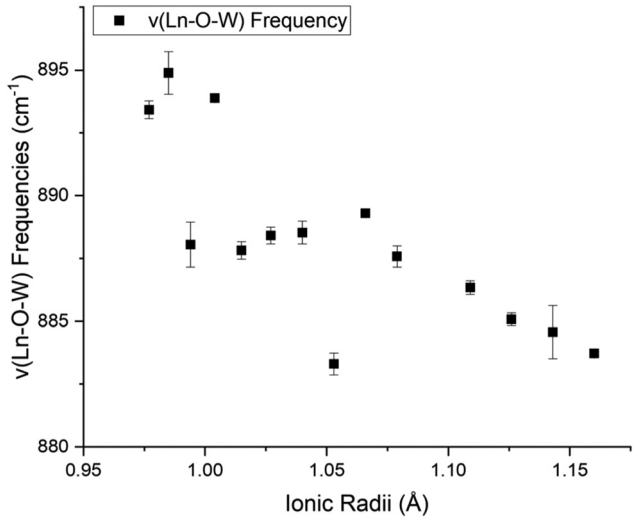

Fig. 10 Plot of Raman ν(Ln–O–W) frequencies *versus* lanthanide ionic radii for complexes **1–14**. Error bars represent uncertainties of the peak center obtained from the fitting regime.

More generally, we have found that FIR and Raman vibrational modes display some correlations between their frequencies and both the ionic radii and the distortion parameters, suggesting these vibrational modes are affected by both the first and second coordination spheres within LnW_{10} POM complexes.

To improve understanding of how structural parameters impact vibrational modes relevant to spin–phonon coupling processes, partial least square (PLS) analysis was done with structural parameters (ionic radii, SA, PA, and PD) as independent variables and each vibrational mode set as the dependent variables (Fig. S56–S66, ESI†). The PLS analysis for the $\nu(WO_5)_2$ FIR stretch shows only two structural parameters, ionic radii and PAs, are statistically significant which is defined by having a variable influence on projection (VIP) value of over 0.8 (Fig. S56 and 57, ESI†); however, the leave-one-out cross validation test which determined the optimal number of independent variables *via* calculation of the minimum root mean PRESS (predicted residual sum of squares), found only one factor, the ionic radii, to be optimal for the fit. The model constructed with only lanthanide ionic radii as the independent variable accounts for 38% of the variance in the $\nu(WO_5)_2$ frequencies. If both structural parameters (ionic radii and plane angle) are included in the PLS model, this accounts for 47% of the variance observed in the frequency of this FIR mode (Fig. S58 and 59, ESI†). PLS analysis on the $\rho(LnO_8)$ FIR mode shows three structural parameters, ionic radii, PAs and SAs, are statistically significant and a cross validation test on the model confirms that ionic radii and SAs are necessary for the fit even though these two independent variables can only account for 30% of the variance in $\rho(LnO_8)$ frequencies (Fig. S60 and 61, ESI†). The low variance accountability for these modes is not surprising as the visual correlations are not strong; however, this suggests that there are other structural parameters with a more significant role in modulating these mode frequencies. PLS analysis on the $\nu/\rho(LnO_8)$ FIR mode finds that three structural parameters, ionic radii, PAs, and SAs, are statistically significant and account for 86% of the variance observed (Fig. S62 and 63, ESI†), which suggests that the $\nu/\rho(LnO_8)$ mode is strongly correlated with these specific structural parameters. This is notable as Blockmon *et al.* found significant coupling between this mode and the $M_J = \pm 7$ states of Ho(III) in HoW_{10}.[31] Moreover, as frequencies of this mode can be modulated by tuning POM structural parameters, this provides a pathway for affecting the extent of spin–phonon coupling within POM complexes by controlling the extent of distortion around the metal center. For the ν(Ln–O–W) Raman mode, PLS analysis indicates that the lanthanide ionic radii is the only statistically significant structural parameter, accounting for 51% of the variance observed in the mode frequency (Fig. S64 and 65, ESI†). This is surprising due to the presence of polymorph based correlations in comparisons between ν(Ln–O–W) mode frequencies and structural distortion parameters that, based on the results from the FIR modes, imply some involvement of the distortion parameters in modulating this mode. Finally, PLS analysis on the [δ(W–O–W/W=O/Ln–O–W)] mode found that none of the structural parameters discussed were a determinant for this vibrational mode (Fig. S66, ESI†). Despite the limited accountability for the variance found in the vibrational modes that were probed using PLS analysis, the models still confirm the involvement of structural parameters in modulating these bands, except for the [δ(W–O–W/W=O/Ln–O–W)] mode, which agrees with the conclusions from our qualitative analysis.

Conclusions

Herein we provide details on fourteen LnW_{10} complexes that were synthesized, structurally analyzed by SCXRD, and characterized using Raman, MIR, and FIR spectroscopies. LnW_{10} POMs have been studied previously; however, we were able to synthesize four new members of the series and identify three new structural polymorphs that have not been previously described. With a complete series of complexes, we were able to probe how POM structural distortion parameters evolve as a function of the lanthanide cation, and we observed polymorph specific trends in distortion parameter data that suggest the second coordination sphere plays a major role in modulating the effective symmetry and the crystal field of the Ln(III) metal center. These findings support the conclusions of Vonci *et al.* who highlighted how using different counter cations could be a pathway to manipulate metal-ion spin states in POM materials,[27] and they also provide a potential structural explanation for why only the HoW_{10} species displays atomic clock transitions as it possesses a unique set of distortion parameters which distinguish it from the other non-Kramers ions in the series. Here we also compiled a library of the vibrational spectra for the entire LnW_{10} series in Raman, MIR, and FIR spectral windows and provided vibrational mode assignments.

Investigation into the correlations between FIR and Raman vibrational modes and structural parameters were done by means of qualitative and PLS analysis, and we found that the FIR modes displayed correlations with both the lanthanide ionic radii and complex distortion parameters whereas for the Raman modes only the ν(Ln–O–W) stretch exhibited a relationship with structural characteristics of complexes **1–14**. Overall, we have shown that structural distortion parameters and the vibrational landscape of LnW_{10} complexes are modulated by changes in the size of the lanthanide metal center and the composition of the lattice. Both of these factors lead to different structural polymorphs, wherein interactions between POM complexes and the second coordination sphere change, and improving understanding of how second sphere interactions impact spin based properties of f-element POM complexes properties will be critical for advancing efforts to tune metal complex crystal fields and control vibronic coupling processes with the spin bath. We are currently working on multiple systems that are focused on exploring how second sphere interactions affect properties related to QIS and reports on the structural, vibrational, and magnetic properties of 4f- and 5f-POM complexes that address this area of research are in progress.

Conflicts of interest

The authors declare no competing interests.

Acknowledgements

This work was primarily supported by the U.S. Department of Energy, Office of Science, Office of Basic Energy Sciences, Early Career Research Program under Award DE-SC0024035. KPC and PJS also acknowledge support from start-up funds from the College of Liberal Arts and Sciences and the Department of Chemistry at the University of Iowa. PJS would also like to thank University of Iowa Graduate College for a 2023 Summer Research Fellowship. We acknowledge the University of Iowa Materials, Analysis, Testing, and Fabrication Facility for use of single crystal and powder X-ray diffractometers as well as the Raman microscope used in this study. Single crystal XRD data was collected on an instrument funded by NSF Award CHE-1828117.

References

1 *Polyoxometalate Molecular Science*, ed. J. J. Borrás-Almenar, E. Coronado, A. Müller and M. Pope, Springer, Dordrecht, Netherlands, 2003.
2 R. J. Errington, in *Polyoxometalate Chemistry From Topology via Self-Assembly to Applications*, ed. M. T. Pope and A. Müller, Springer, Dordrecht, Netherlands, 2001, pp. 7–22.
3 J.-C. Liu, J.-W. Zhao, C. Streb and Y.-F. Song, *Coord. Chem. Rev.*, 2022, **471**, 214734.
4 Y.-F. Song and R. Tsunashima, *Chem. Soc. Rev.*, 2012, **41**, 7384–7402.
5 A. R. Bagheri, N. Aramesh, J. Chen, W. Liu, W. Shen, S. Tang and H. K. Lee, *Anal. Chim. Acta*, 2022, 339509.
6 Q. Liu and X. Wang, *Matter*, 2020, **2**, 816–841.
7 J.-X. Liu, X.-B. Zhang, Y.-L. Li, S.-L. Huang and G.-Y. Yang, *Coord. Chem. Rev.*, 2020, **414**, 213260.
8 Y. Zhang, J. Liu, S.-L. Li, Z.-M. Su and Y.-Q. Lan, *EnergyChem*, 2019, **1**, 100021.
9 A. Bijelic, M. Aureliano and A. Rompel, *Angew. Chem., Int. Ed.*, 2019, **58**, 2980–2999.
10 C. Boskovic, *Acc. Chem. Res.*, 2017, **50**, 2205–2214.
11 M. Ammam, *J. Mater. Chem. A*, 2013, **1**, 6291–6312.
12 M. N. Sokolova, A. M. Fedosseev, G. B. Andreev, N. A. Budantseva, A. B. Yusov and P. Moisy, *Inorg. Chem.*, 2009, **48**, 9185–9190.
13 J.-H. Ding, Y.-F. Liu, Z.-T. Tian, P.-J. Lin, F. Yang, K. Li, G.-P. Yang and Y.-G. Wei, *Inorg. Chem. Front.*, 2023, **10**, 3195–3201.
14 I. Colliard, J. R. Lee, C. A. Colla, H. E. Mason, A. M. Sawvel, M. Zavarin, M. Nyman and G. J.-P. Deblonde, *Nat. Chem.*, 2022, **14**, 1357–1366.
15 G. Aromí and O. Roubeau, in *Handbook on the Physics and Chemistry of Rare Earths*, ed. J.-C. G. Bünzli and V. K. Pecharsky, Elsevier, 2019, vol. 56, pp. 1–54.
16 J. Baldoví, S. Cardona-Serra, A. Gaita-Ariño and E. Coronado, in *Advances in Inorganic Chemistry*, ed. R. van Eldik and L. Cronin, Academic Press, 2017, vol. 69, pp. 213–249.
17 M. Vonci and C. Boskovic, *Aust. J. Chem.*, 2014, **67**, 1542–1552.
18 R. Copping, C. Talbot-Eeckelaers, D. Collison, M. Helliwell, A. J. Gaunt, I. May, S. D. Reilly, B. L. Scott, R. D. McDonald and O. A. Valenzula, *Dalton Trans.*, 2009, 5609–5611.
19 M. R. Antonio and M.-H. Chiang, *Inorg. Chem.*, 2008, **47**, 8278–8285.
20 J. J. Baldoví, L. E. Rosaleny, V. Ramachandran, J. Christian, N. S. Dalal, J. M. Clemente-Juan, P. Yang, U. Kortz, A. Gaita-Ariño and E. Coronado, *Inorg. Chem. Front.*, 2015, **2**, 893–897.
21 J. J. Baldovi, J. M. Clemente-Juan, E. Coronado, Y. Duan, A. Gaita-Ariño and C. Giménez-Saiz, *Inorg. Chem.*, 2014, **53**, 9976–9980.
22 M. Martínez-Pérez, S. Cardona-Serra, C. Schlegel, F. Moro, P. Alonso, H. Prima-García, J. Clemente-Juan, M. Evangelisti, A. Gaita-Ariño and J. Sesé, *Phys. Rev. Lett.*, 2012, **108**, 247213.
23 M. Jenkins, Y. Duan, B. Diosdado, J. J. García-Ripoll, A. Gaita-Ariño, C. Giménez-Saiz, P. J. Alonso, E. Coronado and F. Luis, *Phys. Rev. B*, 2017, **95**, 064423.
24 M. Shiddiq, D. Komijani, Y. Duan, A. Gaita-Ariño, E. Coronado and S. Hill, *Nature*, 2016, **531**, 348–351.
25 S. Giménez-Santamarina, S. Cardona-Serra, J. M. Clemente-Juan, A. Gaita-Arino and E. Coronado, *Chem. Sci.*, 2020, **11**, 10718–10728.

26 J. T. Muhonen, J. P. Dehollain, A. Laucht, F. E. Hudson, R. Kalra, T. Sekiguchi, K. M. Itoh, D. N. Jamieson, J. C. McCallum and A. S. Dzurak, *Nat. Nanotechnol.*, 2014, **9**, 986–991.
27 M. Vonci, M. J. Giansiracusa, W. Van den Heuvel, R. W. Gable, B. Moubaraki, K. S. Murray, D. Yu, R. A. Mole, A. Soncini and C. Boskovic, *Inorg. Chem.*, 2017, **56**, 378–394.
28 K. Kundu, J. Chen, S. Hoffman, J. Marbey, D. Komijani, Y. Duan, A. Gaita-Ariño, J. Stanton, X. Zhang and H.-P. Cheng, *Commun. Phys.*, 2023, **6**, 38.
29 K. Kundu, J. R. White, S. A. Moehring, J. M. Yu, J. W. Ziller, F. Furche, W. J. Evans and S. Hill, *Nat. Chem.*, 2022, **14**, 392–397.
30 S. Ghosh, S. Datta, L. Friend, S. Cardona-Serra, A. Gaita-Ariño, E. Coronado and S. Hill, *Dalton Trans.*, 2012, **41**, 13697–13704.
31 A. L. Blockmon, A. Ullah, K. D. Hughey, Y. Duan, K. R. O'Neal, M. Ozerov, J. J. Baldoví, J. Aragó, A. Gaita-Ariño and E. Coronado, *Inorg. Chem.*, 2021, **60**, 14096–14104.
32 R. Mirzoyan, N. P. Kazmierczak and R. G. Hadt, *Chem. – Eur. J.*, 2021, **27**, 9482–9494.
33 O. Y. Mariichak, S. Kaabel, Y. A. Karpichev, G. M. Rozantsev, S. V. Radio, C. Pichon, H. Bolvin and J.-P. Sutter, *Magnetochemistry*, 2020, **6**, 53.
34 O. Y. Mariichak, V. Ignatyeva, V. Baumer, G. Rozantsev and S. Radio, *J. Chem. Crystallogr.*, 2020, **50**, 255–266.
35 L. E. Roy, D. Ortiz-Acosta, E. R. Batista, B. L. Scott, M. W. Blair, I. May, R. E. Del Sesto and R. L. Martin, *Chem. Commun.*, 2010, **46**, 1848–1850.
36 K. Sawada and T. Yamase, *Acta Crystallogr., Sect. C: Cryst. Struct. Commun.*, 2002, **58**, i149–i151.
37 T. Ozeki and T. Yamase, *Acta Crystallogr., Sect. C: Cryst. Struct. Commun.*, 1994, **50**, 327–330.
38 M. Sugeta and T. Yamase, *Bull. Chem. Soc. Jpn.*, 1993, **66**, 444–449.
39 J. J. Baldovi, S. Cardona-Serra, J. M. Clemente-Juan, E. Coronado, A. Gaita-Arino and A. Palii, *Inorg. Chem.*, 2012, **51**, 12565–12574.
40 M. A. AlDamen, S. Cardona-Serra, J. M. Clemente-Juan, E. Coronado, A. Gaita-Arino, C. Marti-Gastaldo, F. Luis and O. Montero, *Inorg. Chem.*, 2009, **48**, 3467–3479.
41 R. Shiozaki, A. Inagaki, A. Nishino, E. Nishio, M. Maekawa, H. Kominami and Y. Kera, *J. Alloys Compd.*, 1996, **234**, 193–198.
42 J. G. Kragskow, J. Marbey, C. D. Buch, J. Nehrkorn, M. Ozerov, S. Piligkos, S. Hill and N. F. Chilton, *Nat. Commun.*, 2022, **13**, 825.
43 D. H. Moseley, S. E. Stavretis, Z. Zhu, M. Guo, C. M. Brown, M. Ozerov, Y. Cheng, L. L. Daemen, R. Richardson and G. Knight, *Inorg. Chem.*, 2020, **59**, 5218–5230.
44 *APEX4*, Bruker AXS Inc., Madison, WI, USA, 2022.
45 L. Krause, R. Herbst-Irmer, G. M. Sheldrick and D. Stalke, *J. Appl. Crystallogr.*, 2015, **48**, 3–10.
46 G. M. Sheldrick, *Acta Crystallogr., Sect. A: Found. Adv.*, 2015, **71**, 3–8.
47 G. M. Sheldrick, *Acta Crystallogr., Sect. C: Struct. Chem.*, 2015, **71**, 3–8.
48 O. V. Dolomanov, L. J. Bourhis, R. J. Gildea, J. A. Howard and H. Puschmann, *J. Appl. Crystallogr.*, 2009, **42**, 339–341.
49 D. Palmer, *CrystalMaker*, CrystalMaker Software Ltd, Begbroke, Oxfordshire, England, 2014.
50 B. Lottes and K. P. Carter, *Chem. – Eur. J.*, 2023, **29**, e202300749.
51 A. E. Gelfand, D. K. Dey and H. Chang, *Model Determination Using Predictive Distributions with Implementation via Sampling-Based Methods*, Technical Report No. 462, U.S. Office of Naval Research, 1992.
52 P. Geladi and B. R. Kowalski, *Anal. Chim. Acta*, 1986, **185**, 1–17.
53 J. M. Andrade-Garda, A. Carlosena-Zubieta, R. Boqué-Martí and J. Ferré-Baldrich, in *Basic Chemometric Techniques in Atomic Spectroscopy*, ed. J. M. Andrade-Garda, The Royal Society of Chemistry, Cambridge, United Kingdom, 2013, pp. 280–347.
54 *OriginPro, Version 2023b*, Origin Lab Corporation, Northampton, MA, USA.
55 R. D. Shannon, *Acta Crystallogr., Sect. A: Cryst. Phys., Diffr., Theor. Gen. Crystallogr.*, 1976, **32**, 751–767.
56 R. Peacock and T. Weakley, *J. Chem. Soc. A*, 1971, 1836–1839.
57 B. George, G. Aruldhas and I. L. Botto, *J. Mater. Sci. Lett.*, 1992, **11**, 1421–1423.
58 M. A. AlDamen, J. M. Clemente-Juan, E. Coronado, C. Martí-Gastaldo and A. Gaita-Arino, *J. Am. Chem. Soc.*, 2008, **130**, 8874–8875.
59 A. Gaita-Ariño, F. Luis, S. Hill and E. Coronado, *Nat. Chem.*, 2019, **11**, 301–309.
60 J. J. Baldoví, S. Cardona-Serra, J. M. Clemente-Juan, E. Coronado and A. Gaita-Ariño, *Chem. Sci.*, 2013, **4**, 938–946.
61 L. Kazanskii, A. Golubev, I. Baburina, E. Torchenkova and V. Spitsyn, *Bull. Acad. Sci. USSR, Div. Chem. Sci.*, 1978, **27**, 1956–1960.
62 D. C. Harris and M. D. Bertolucci, *Symmetry and Spectroscopy: An Introduction to Vibrational and Electronic Spectroscopy*, Dover Publications, Inc., New York, NY, USA, 1989.
63 E. L. Kendix, PhD thesis, University of Bologna, 2009.